coatings

MDPI

Article

Effect of Alternating Magnetic Field on the Organization and Corrosion Resistance of 2205 Duplex Stainless Steel Narrow-Gap Laser-MIG Hybrid Weld Head

Zhenxing He [1], Yong Zhao [1,*], Juan Fu [1], Fugang Chen [1], Guoqiang Chen [2] and Yonghui Qin [2]

[1] Provincial Key Lab of Advanced Welding Technology, Jiangsu University of Science and Technology, Zhenjiang 212003, China; 211210601107@stu.just.edu.cn (Z.H.); fujuan@just.edu.cn (J.F.); chenfugang@just.edu.cn (F.C.)
[2] Jiangsu Yangzi-Mitsui Shipbuilding Co., Ltd., Taicang 215400, China; chenguoqiang@yzjship.com (G.C.); qyh@yzjship.com (Y.Q.)
* Correspondence: yongzhao418@just.edu.cn; Tel.: +86-13815485895

Abstract: In this study, an alternating magnetic field is applied in the narrow-gap laser-MIG hybrid welding of 2205 duplex stainless steel with a thickness of 25 mm to achieve the purpose of balancing the ration of the two phases, refining the grains and improving the corrosion resistance. With the help of OM, EBSD, TEM, and other microstructural analysis methods, the organization evolution of a 2205 duplex stainless steel narrow-gap laser arc hybrid weld under the effect of alternating magnetic field is revealed. The corrosion resistance of the welded joints is investigated by electrochemical tests. The results show that the use of a 40 mT applied alternating magnetic field can not only effectively inhibit the generation of porosity and unfused defects in the weld, but also that the addition of an alternating magnetic field improves the ratio of austenite to ferrite in the weld, and the ratio of the two phases is increased from 0.657 without a magnetic field to 0.850. The weld grain preferential orientation is affected by the magnetic field, and the weld austenite grains are shifted from the Goss texture to the Copper texture. Under the electromagnetic stirring effect of the applied magnetic field, the average austenite grain size decreased from 4.15 μm to 3.82 μm, and the average ferrite grain size decreased from 4.99 μm to 4.08 μm. In addition, the effect of the alternating magnetic field increases the density of twins in the organization. Electrochemical test results show that the addition of an alternating magnetic field increases the corrosion potential by 75.2 mV and the pitting potential by 134.5 mV, which indicates that the corrosion resistance of the cover-welded specimens is improved by the effect of an alternating magnetic field. The improvement in corrosion resistance mainly depends on the austenite grain refinement and the increase in the austenite content.

Keywords: duplex stainless steel; alternating magnetic field; laser-MIG hybrid welding; microstructure evolution; corrosion

Citation: He, Z.; Zhao, Y.; Fu, J.; Chen, F.; Chen, G.; Qin, Y. Effect of Alternating Magnetic Field on the Organization and Corrosion Resistance of 2205 Duplex Stainless Steel Narrow-Gap Laser-MIG Hybrid Weld Head. *Coatings* **2023**, *13*, 2000. https://doi.org/10.3390/coatings13122000

Academic Editor: Giuseppina Raffaini

Received: 8 November 2023
Revised: 20 November 2023
Accepted: 21 November 2023
Published: 24 November 2023

1. Introduction

Duplex stainless steel fully combines the advantages of austenitic and ferritic stainless steels due to the similar ratio of austenitic (γ) phase and ferrite (δ) in its microstructure [1,2]. As an iron-based alloy with both austenitic and ferritic organizations, it has both excellent mechanical properties and corrosion resistance. Therefore, it is widely used in production conditions such as oil storage and transportation, natural gas plants, and desalination plants [3,4]. Fusion welding is one of the commonly used traditional welding processes. However, due to the high heat input and fast cooling rate of the welding process, two-phase organization imbalance and joint property deterioration are prone to occur after the welding of duplex stainless steel [5,6]. High-energy density welding processes, such as narrow-gap laser-MIG hybrid welding, have received widespread attention due to the advantages of a small bevel size, less filler metal, a high welding efficiency, etc [7,8].

However, during the solidification process of the weld pool in narrow-gap laser-MIG hybrid welding, the laser energy mainly gathers at the bottom of the weld, and defects such as porosity and unfused welds often appear in the weld [9,10]. Therefore, it is necessary to adopt a practical and effective welding method to inhibit the generation of defects. Wang et al. [11] utilize a magnetic field to rotate the arc within a narrow-gap bevel, avoiding unfused defects through changes in energy distribution. Similarly, the magnetic field-assisted welding method also has an obvious inhibiting effect on porosity defects [12–15]. According to previous studies, the addition of a magnetic field to optimize the molten pool fluidity during the welding process is considered to be an effective way to improve the quality of welded joints [16–18]. Fu et al. [19] used laser arc hybrid welding of an S32101 duplex stainless steel plate under the magnetic field generated by Nd-Fe-B permanent magnets. The welding process is analyzed by high-speed imaging and spectral analysis. The results show that not only can the plasma temperature be increased under the effect of the magnetic field, but also that the melt pool flow is more uniform under a certain magnetic field strength. Applying the magnetic field assistance in the welding process and utilizing the electromagnetic stirring (EMS) effect generated by the magnetic field can achieve the purpose of refining the grain [20,21] and balancing the ratio of the two phases [22–24]. Zhu et al. [25] applied a perpendicular magnetic field in 316 L narrow-gap laser-MIG hybrid welding. The magnetic field ampere force was utilized to change the convection flow in the molten pool, causing the ferrite to remelt by dendrite fracture. In addition, the corrosion resistance of the metal is also very important [26]. Magnetic fields are used in the fusion welding of duplex stainless steel to improve the resistance to localized corrosion by using a low-intensity magnetic field assist [27]. Zhong et al. [28] utilized a novel in-situ transverse magnetic field acting on a cold metal transfer in a directional energy deposition arc of 316 L stainless steel. Under the action of the magnetic field, the Cr and Ni metal oxides in the passivation film increased significantly, and the stability of the passivation film was improved.

The addition of a magnetic field changes the distribution of the weld heat source, which affects the organization and properties [29]. Studies related to alternating magnetic fields are rare, and the use of magnetic field effects to improve organization and properties is valuable. In this study, 25 mm thick 2205 duplex stainless steel is selected as the base material, and an alternating magnetic field parallel to the weld is applied to narrow-gap laser-MIG hybrid welding. The effects of the alternating magnetic field on the two-phase equilibrium of the weld tissue, the distribution of the texture, the grain orientation, and the grain size are discussed via OM, EBSD, and TEM [30]. To elucidate the mechanism of the tissue structure transformation under the effect of alternating magnetic fields [31], we analyze the effect of an alternating magnetic field on the corrosion resistance of 2205 duplex stainless steel welded joints with narrow-gap laser arc hybrid welding through electrochemical tests. The effect of the alternating magnetic field on the organization characteristics and corrosion resistance of laser-MIG hybrid welded joints of duplex stainless steel is illustrated according to the test results. The roadmap for the paper is shown in Figure 1.

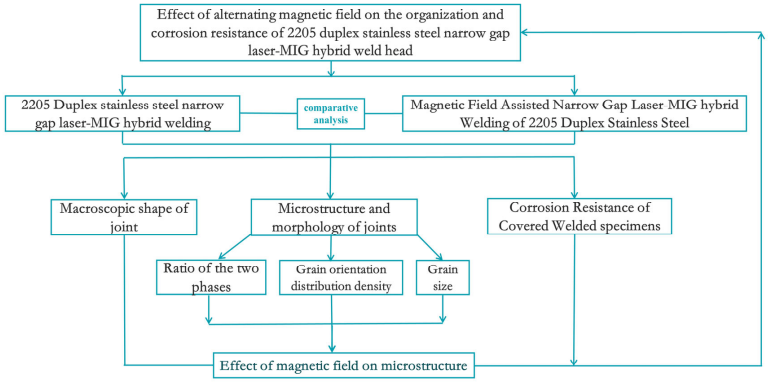

Figure 1. The roadmap for the paper.

2. Experimental Procedure

2.1. Base Material and Welding Procedure

In this study, a 25 mm thick 2205 duplex stainless steel plate is used as the base material, and the filler wire is selected as an ER2209 stainless steel solid wire with a diameter of 1.2 mm. The chemical composition of DSS2205 and ER2209 is shown in Table 1.

Table 1. Main chemical composition of DSS2205 and ER2209 (wt.%).

Material	C	S	P	Ni	Cr	Mo	N	Mn	Si	Fe
2205	0.024	0.001	0.023	5.68	22.39	3.13	0.17	1.38	0.39	Bal.
ER2209	0.019	0.0008	0.016	9.41	22.59	3.1	0.16	1.66	0.17	Bal.

In this study, the welding system consists of a YLS-6000 fiber laser generator (wavelength 1065–1080 nm), a Kuka robot, and a Fronius TPS500i PLUSE-type intelligent arc welding power system (Fronius welding Tech., Ltd., Zhuhai, China). Multi-position welding can be realized by a KUKA 6-axis robot. A fiber optic transmission system delivers the laser to the laser head and the welding is carried out using a KUKA industrial robot equipped with a laser head, wire feed mechanism, and protective gas unit. The alternating magnetic field generating equipment is an 8080 magnetic field controller from Jetline Engineering (Irvine, CA, USA) with a 4604 head. The alternating magnetic field assisted 25 mm thick 2205 duplex stainless steel narrow-gap laser-MIG hybrid welding equipment and groove size schematic are shown in Figure 2.

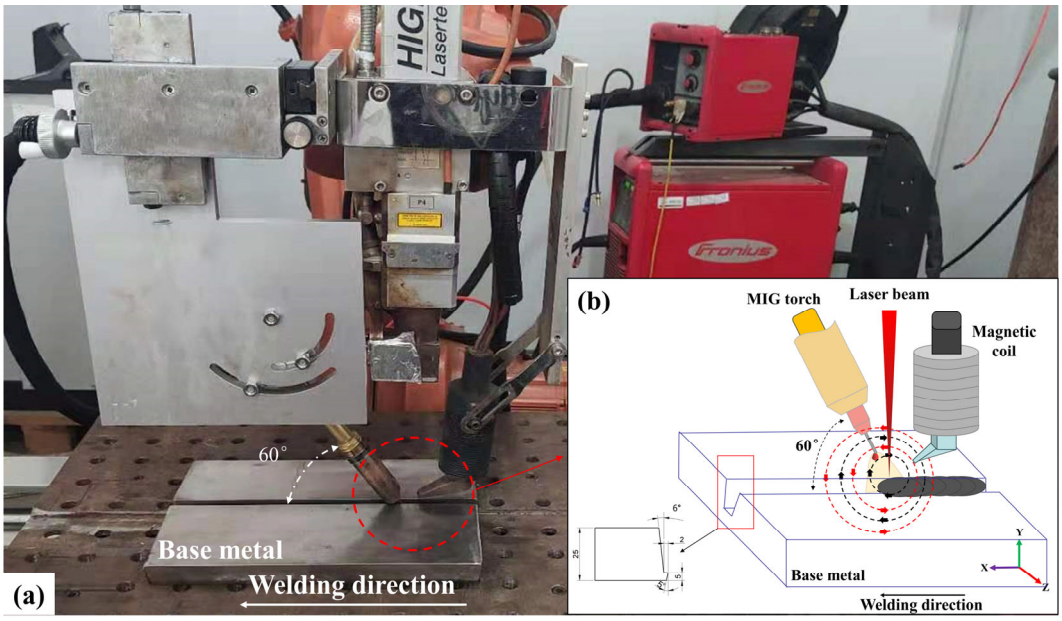

Figure 2. Schematic representation of the test setup and welding process: (**a**) Alternating magnetic field assisted narrow-gap laser arc hybrid welding test platform; (**b**) Schematic diagram of the test process and groove dimensions.

The size of the magnetic field strength and frequency can be changed by adjusting the magnetic field frequency and magnetic field amplitude knobs on the magnetic field controller, and by acting on the arc through the magnetic head, the regulation of the transition of the molten droplet and the flow of the molten pool can be realized. In the welding process, the magnetic field equipment can provide the highest alternating magnetic field frequency of 50 Hz, and the maximum alternating magnetic induction strength of 60 mT. The laser-MIG hybrid welding parameters are shown in Table 2. A magnetic field

strength of 40 mT is chosen, which is measured by means of a Gauss meter. The magnetic field frequency is 15 Hz.

Table 2. Welding parameters of 25 mm DSS narrow-gap laser arc hybrid welding.

No.	P (kW)	I (A)	V (m/min)	Δf (mm)	D_{LA} (mm)	B (mT)	f (Hz)
1	2.3	220					
2	2.0	220					
3~4	2.0	240	0.8	+5	2	40	15
5~6	2.0	260					
7	1.7	240					

2.2. Microstructure Characterization

In this paper, the macroscopic morphology and microstructure of the welds are observed and analyzed by a 3D macroscope and metallurgical microscope, and Image Pro 6.0 image processing software is applied to statistically calculate the ratio of ferrite and austenite phases in different regions. The specimens are corroded with Beraha's reagent (0.5 g $K_2S_2O_5$ + 20 mL HCl + 80 mL of deionized water) after abrasive polishing and the duration of the corrosion is 5 to 10 s. The EBSD specimens are coarsely polished and then finely polished with a 50 nm SiO_2 suspension until there are no scratches under a 500× microscope, and vibratory polishing is used to remove the small amount of deformation and residual stresses left behind by the mechanical polishing. A Merlin Compact scanning electron microscope (Carl ZEISS Microscopy GmbH, Oberkochen, Germany) is used for the EBSD test with a test scan step of 1 μm, and the characteristics of the specimens' texture and grain orientation are comparatively analyzed by using Channel 5 software with and without the effect of an alternating magnetic field. A JEM-2100F field emission transmission electron microscope (TEM, JEOL, Tokyo, Japan) is used to analyze the two-phase deformation mechanism and interface morphology within the weld.

2.3. Corrosion Testing

Electrochemical tests are conducted using a three-electrode system, and the CS-2350H electrochemical workstation is used for electrochemical testing. A weld specimen of size 10 × 10 × 5 mm is prepared, and the copper conductor is fixed with the specimen using double-sided conductive copper foil tape and cold set with epoxy resin and then polished. The corrosion medium is artificial seawater (26.5 g/L NaCl, 24 g/L $MgCl_2$, 0.73 g/L KCl, 3.3 g/L $MgSO_4$, 0.2 g/L $NaHCO_3$, 1.1 g/L $CaCl_2$ and 0.28 g/L NaBr.). Before testing, to ensure the stability of the specimens in the medium, the specimens are placed in a simulated seawater medium for 0.5 h to ensure that there are no abnormal fluctuations in the open-circuit potential. The dynamic potential scanning range is −0.2 V~1.5 V, the rate is 0.333 mV/s, and the test temperature is 20 °C.

3. Results and Discussion

3.1. Weld Shaping and Microstructure Morphology

The shape of the narrow-gap laser-MIG hybrid weld seam assisted by an alternating magnetic field is shown in Figure 3. Under the effect of no magnetic field, the weld bead appears as a biting edge phenomenon, while the weld seam is smooth and beautiful in the case of an assisted magnetic field. Referring to the standard NB/T47013, X-ray nondestructive testing of the weld was performed. There are many pores and unfused defects inside the weld without a magnetic field. In contrast, there are no obvious defects inside the weld under a certain intensity and frequency. This is because the addition of the magnetic field produces an electromagnetic stirring effect on the molten pool, which increases the molten pool fluidity and is conducive to the overflow of porosity. At the same time, the magnetic field increases the plasma temperature, which effectively reduces the generation of unfused defects. This has been pointed out in the study of Cai et al. [32].

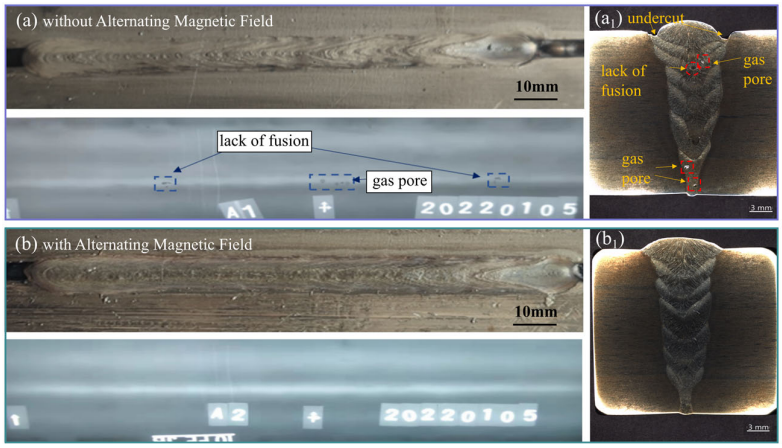

Figure 3. Welded joint forming and macroscopic morphology: (**a**,**a**$_1$) without alternating magnetic field; (**b**,**b**$_1$) with alternating magnetic field.

Narrow-gap laser arc hybrid welded joints for thick plates can be divided into four areas: the cosmetic bead, the filling bead, the overlapping bead, and the heat-affected zone. The organization and two-phase ratios of the four zones are analyzed. For the selected specimens, 10 collection locations are randomly selected to ensure that the collection area would cover most of the microstructure metallograph. The relative content of austenite and ferrite is measured using Image Pro Plus 6.0 software. The relative contents of austenite and ferrite are averaged over the 10 acquisition locations as shown in Table 3.

Table 3. Statistical table of two-phase organization score measurements.

Magnetic Field	Phase (%)	CB	FB	OB	HAZ
Without AMF	γ	36.5	40.1	46.1	35.7
	δ	63.5	59.9	53.9	64.3
With AMF	γ	39.9	43.4	53.6	40.2
	δ	60.1	56.6	46.4	59.8

In this paper, for illustrative purposes, the ratio of the relative austenite content to relative ferrite content is denoted as Y. The closer Y is to 1, the more balanced is the ratio of the two phases. The microstructure is shown in Figure 4.

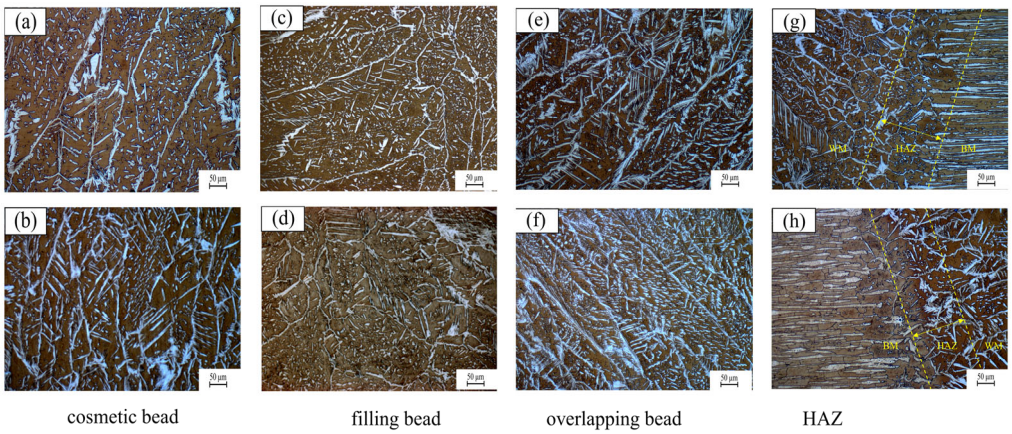

Figure 4. Microstructure and morphology: (**a**,**c**,**e**,**g**) without alternating magnetic field; (**b**,**d**,**f**,**h**) with alternating magnetic field.

Figure 4a shows the microstructure of the cosmetic bead without magnetic field assistance. Under the magnetic field, as in Figure 4b, the two-phase homogeneity is

improved from 0.575 to 0.664. Higher homogeneity occurs in filler weld passes, as in Figure 4c,d, which is attributed to the combined effect of the magnetic field and preheating of the previous weld beads, which retards the solid-state phase transformation. The continuous nucleation of austenite increases the Y from 0.669 to 0.767 in the organization of the filling beads under a magnetic field. In multi-layer multi-pass welding, the overlap zone is affected by in-heating tempering, and there will be secondary austenite (γ_2) produced, which is distributed in the γ_1 primary austenite grain boundaries, with γ_1 expanding into the ferrite grains; γ_2 is finer in size, and the adjacent γ_2 shows a twin-crystal organization.

The austenite phase interface is very dense under the effect of an alternating magnetic field, and the organizational characteristics are dominated by the austenite phase. Figure 4f shows the organization and morphology under the alternating magnetic field, in which there is grain boundary austenite with continuous nucleation growth along the ferrite phase interface. There is densely present parallel lath-like Widmanstätten austenite, and dense intragranular austenite is also present within the grains. In addition, the stirring effect of the alternating magnetic field exacerbates the energy changes inside the molten pool, which promotes the precipitation of fine austenite within the ferrite grains in a non-diffusive transformation. Calculation of the two-phase homogeneity of austenite/ferrite in overlapping beads showed a two-phase homogeneity Y of 0.855 without the alternating magnetic field and Y of 1.160 with the applied magnetic field.

The heat-affected zone is not significantly affected by the magnetic field, but the homogeneity also increases from 0.555 to 0.672. The average two-phase homogeneity of the combined four zones improves from 0.663 to 0.816, which is closer to 1.0. This indicates that the effect of the alternating magnetic field leads to a more balanced ratio of the two phases after welding. Increased homogeneity of the two phases can improve the strength and plasticity of duplex stainless steel.

3.2. Distribution of Two-Phase Orientation and Texture in Welds

Figure 5 shows the EBSD phase diagram and the IPF of the cosmetic bead in the presence or absence of an alternating magnetic field. The IPF in the RD direction reflects the grain orientation distribution, and the EBSD phase diagram gives the distribution and content of the austenite and ferrite phases, where ferrite is red and austenite is yellow.

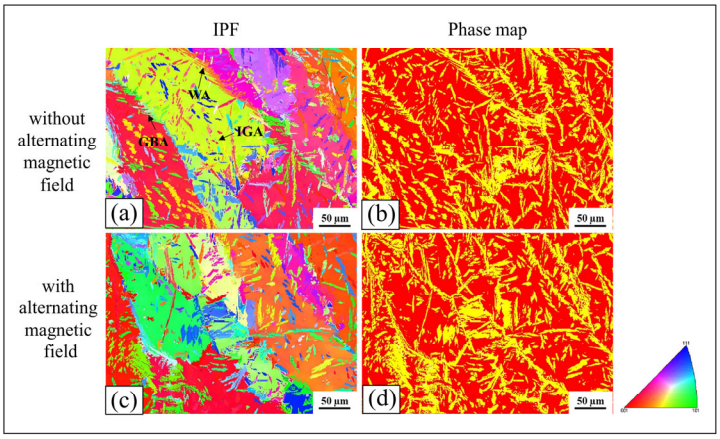

Figure 5. EBSD phase maps and IPFs in the RD direction of the cosmetic bead: (**a**,**b**) without alternating magnetic field; (**c**,**d**) with alternating magnetic field.

In the absence of an alternating magnetic field, the cosmetic bead is mainly a columnar crystal. It grows from the fusion line to the center of the weld. The weld organization mainly exhibits coarse ferrite grains and fine strips of GBA (grain boundary austenite) distributed at the grain boundaries. as shown in Figure 5a. From the grain boundary to the intracrystalline growth of the side plate stripes of WA (Widmanstätten austenite) and intracrystalline fine IGA (intragranular austenite), the overall diffuse distribution, when the ferrite grains

are mainly oriented to (001)//RD. From the IPF of the weld with an applied alternating magnetic field in Figure 5c, it can be found that the weld is still dominated by coarse columnar crystals growing obliquely toward the center of the weld in general. However, the shape of the columnar crystals is irregular, and there is a transversely distributed austenite within the crystals, and the austenite is increased. The grain orientation is also gradually transformed to (101)//RD, and the grain orientation is (001)//RD and (101)//RD.

Comparison of the phase diagrams with and without the effect of an applied alternating magnetic field reveals that in the absence of a magnetic field, elongated GBA is distributed on the ferrite matrix and lath-like WA nucleates at the grain boundaries, and that it grows toward the grain interior. At the same time, IGA precipitates inside the ferrite as shown in Figure 5b. After the application of an alternating magnetic field, part of the region of the grain boundary characteristics became less obvious, the alternating magnetic field in the weld introduced dislocations or twins, which divided the original grain, so that the large-angle grain boundaries were split into a large number of small-angle grain boundaries and the ferrite grain was refined. The austenite phase in the weld grows, part of the austenite phase to the grain growth; there is a tendency to cross the ferrite grain, part of the austenite derived from the secondary austenite; the formation of the austenite phase is a feathery flocculent, as shown in Figure 5d.

Figure 6 shows the pole figure and the IPF of the austenite and ferrite {100}, {110}, and {111} within the weld with and without the action of an alternating magnetic field. The RD surface is usually chosen as the projection surface for the pole figure, and the pole figure is obtained by the pole density distribution. The distribution of grain surfaces on the rolling surface is analyzed by {100}, {110}, and {111} pole figures, and grain orientation is analyzed using the IPF in the RD direction.

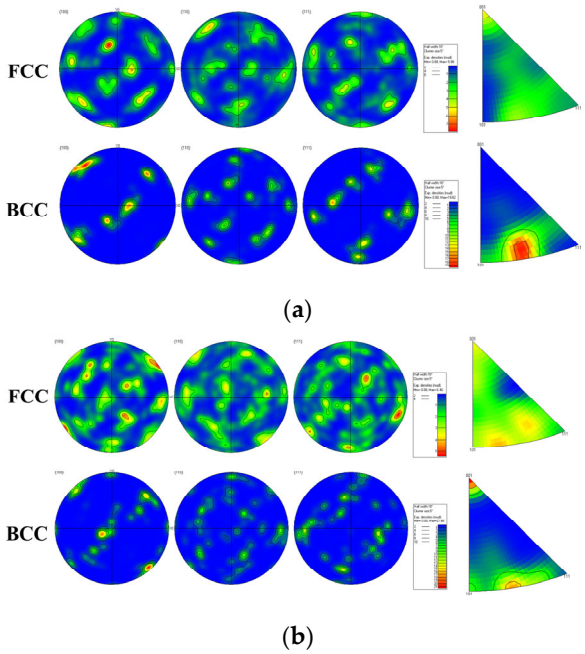

Figure 6. The pole figure and the IPF of austenite and ferrite. (**a**) without alternating magnetic field; (**b**) with alternating magnetic field.

From Figure 6a, it can be seen that in the absence of a magnetic field, there is a partial texture in the austenite, mainly with the {110} plane parallel to the rolling plane. The IPF shows that most of the grains are preferentially oriented in the <001> direction, with a maximum grain orientation distribution density of 5.88. Some dispersed texture also exists in the ferrite, and the main texture shows that the {100} plane is parallel to the rolling plane. The antipodal diagram shows that the preferential orientation of the grains is close to the

<101> direction, and the maximum grain orientation distribution density is 19.82. The pole figure and the IPF of the weld after the application of the alternating magnetic field are shown in Figure 6b, where the austenite weave density of the weld is enhanced under the action of the alternating magnetic field, and the austenite phase exhibits more selective orientations, close to <001>, <101> and gradually shifting to <111> in the direction along the rolling direction. The austenite grains may be shifted from Goss texture to Copper texture, and the grain orientation distribution density increased to 6.46.

After the application of an alternating magnetic field, there is no significant change in the main ferrite texture. However, as shown in the IPF, the grain orientation shifted from <101> to <001>, at which time the grain orientation distribution density increased to 21.60.

3.3. Grain Boundary Orientation Difference and Grain Size of the Weld

According to the difference in the angle of the orientation difference between neighboring grains, grain boundaries can be classified into low angle grain boundaries, LABs (orientation difference <15°) and high angle grain boundaries, HABs (orientation difference >15°), of which HAGBs include normal large angle grain boundaries and coincident site lattice grain boundaries; generally, in austenite often appear [111]/60° of Σ3 coincident lattice [33,34], and the orientation relationship of the two CSLs is twinning, so in this paper, the CSL grain boundaries content will be recognized as Σ3 twinning boundary content.

Figure 7 shows the distribution of the grain boundary orientation difference between the two phases of the cosmetic bead with and without the effect of an alternating magnetic field. Without the effect of alternating magnetic fields, the ferrite phase contains 39.4% LAGBs, 60.6% HAGBs, and the twinned grain boundary is 1.82%. The austenite phase contains 52.7% HAGBs and 3.0% twin boundaries, at which time the grain orientation is easily changed in favor of the Goss texture. After the application of an alternating magnetic field, the HAGBs in the ferrite phase decrease to 44.7%, and the HAGBs in the austenitic phase increase. The effect of the alternating magnetic field impacts the dislocation climbing within the ferrite and reduces the laminar dislocation energy. The action on the austenitic phase favors the formation of twins, increases the grain boundary transition potential, and raises the possibility of a grain orientation change. As a result of the analysis of the contrast pole figure, the austenite grains are transferred from the Goss texture to the Copper texture. The grain size distribution of the two phases of the weld with and without the assistance of the alternating magnetic field is shown in Figure 8. The average grain size of the ferrite phase of the weld without an alternating magnetic field is 4.99 μm, and the average grain size of the austenite phase is 4.15 μm. After the application of the alternating magnetic field, the ferrite phase and the austenite phase are affected by electromagnetic stirring, and the average sizes of the grains of the two phases become smaller, with the ferrite phase decreasing to 4.08 μm, and the austenite phase decreasing to 3.82 μm. It is worth mentioning that the grain refinement increases the weld toughness. The refinement of austenite and the increase in austenite content in the cover organization play a very important role in the improvement of corrosion resistance.

Figure 9 shows the TEM and SEAD with and without a magnetic field. Figure 9a shows the TEM photographs of the weld with no alternating magnetic field, and the twinned organization with elongated lamellar structure throughout the grain is observed within the austenitic organization. Figure 9b shows the TEM pictures of the weld after the introduction of the magnetic field. After the introduction of an alternating magnetic field, the twin density is increased to some extent, which leads to a texture transition when the density reaches a certain level. As a result, twin crystals are more easily formed with the assistance of the alternating magnetic field, and the possibility of grain orientation change is increased.

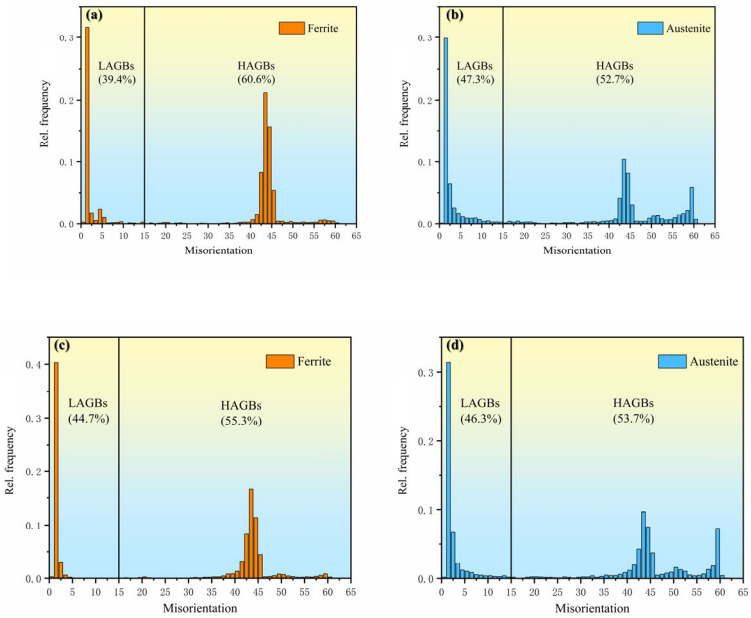

Figure 7. Misorientation angle distribution of grain boundaries of the cosmetic bead: (**a**) Ferrite without alternating magnetic field; (**b**) Austenite without alternating magnetic field; (**c**) Ferrite without alternating magnetic field; (**d**) Austenite without alternating magnetic field.

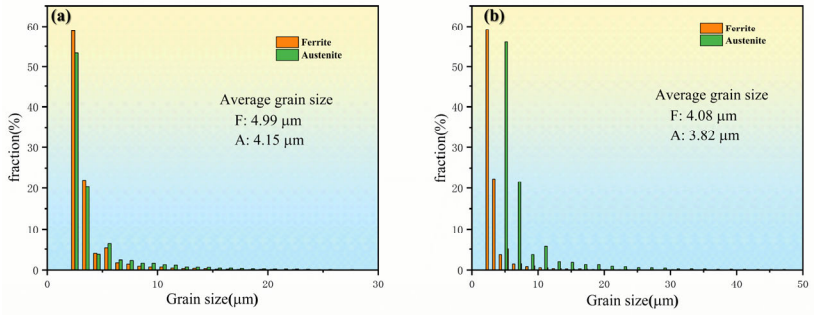

Figure 8. Grain size of the two phases of the weld: (**a**) without alternating magnetic field; (**b**) with alternating magnetic field.

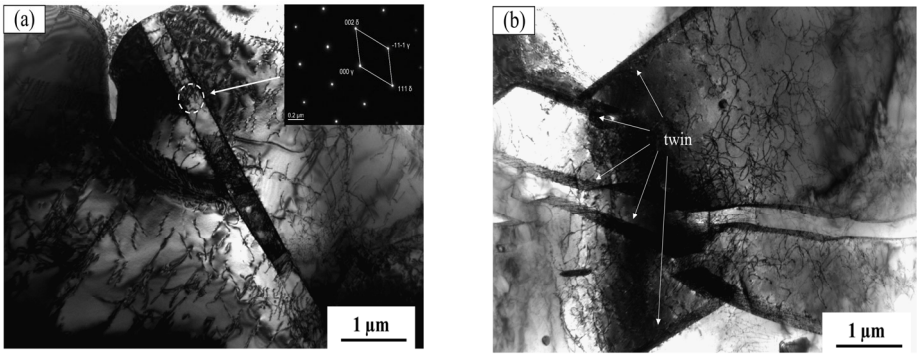

Figure 9. Twin crystal morphology in the weld: (**a**) without alternating magnetic field; (**b**) with alternating magnetic field.

3.4. Potentiodynamic Polarization

Dynamic potential scanning tests are carried out on welds with and without magnetic fields to study the corrosion resistance of the welds. The polarization curves are shown in Figure 10. In the dynamic potential polarization curve test, the corrosion potential (E_{corr}) and corrosion current density (I_{corr}) are commonly used to indicate the dissolution ability

of the metal, which visually reflects the corrosion resistance of the metal under no applied conditions. Theoretically, the higher the value of E_{corr} is, the lower is the value of I_{corr}, indicating that the metal corrosion resistance is better [35]. Pitting corrosion of stainless steel requires special attention and generally occurs at inclusions or grain boundaries [36]. The anodic current undergoes an abrupt change when pitting occurs, and the potential inflection point obtained at this time is the pitting potential (E_b). The higher the pitting potential is, the better is the corrosion resistance of the metal.

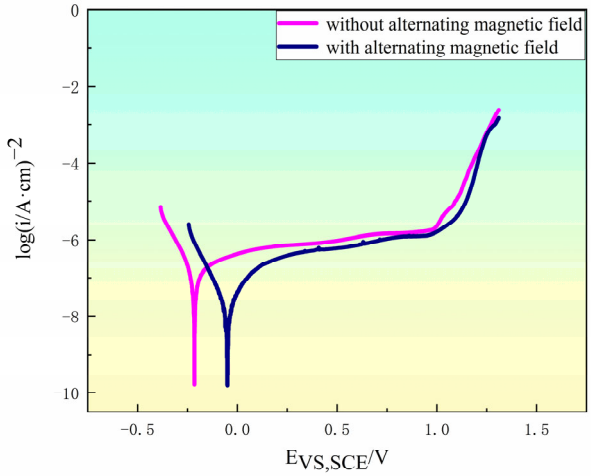

Figure 10. Polarization curve of welded joint in simulated seawater.

Figure 10 shows that the trends of the curves are similar for the welds with and without magnetic field assistance. With the increase in corrosion potential, both specimens experience long passivation intervals and then tend to stabilize. As the corrosion potential continues to rise, the current density of the welded specimen without the effect of an alternating magnetic field is the first to change and enter the over-passivation zone, and pitting corrosion occurs on the metal surface. Comparing the current density at the same corrosion potential, it can be found that the current density of the welded specimen with the applied alternating magnetic field is significantly lower than that without the alternating magnetic field, and the lower corrosion current indicates a slower corrosion rate and better corrosion resistance. Compared with the welded specimens without an alternating magnetic field, the welded specimens with an alternating magnetic field have higher corrosion potential; the pitting potential is obviously larger, which indicates that the 2205 duplex stainless steel welded joints with an alternating magnetic field have better corrosion resistance. The eigenvalue parameters of the dynamic potential polarization curves are obtained by fitting using the Tafel extrapolation method as shown in Table 4.

Table 4. The polarization curve fitting results and corrosion rate of cover welded specimens.

Magnetic Field	E_{corr} (V)	I_{corr} (A·cm^{-2})	E_{pass} (V)	I_{pass} (A·cm^{-2})	E_{pit} (V)	Corrosion Rate (mm/y)
Without AMF	−0.2150	1.82×10^{-7}	0.1439	6.26×10^{-7}	1.1775	2.14×10^{-3}
With AMF	−0.1398	2.64×10^{-8}	0.0637	4.21×10^{-7}	1.312	0.28×10^{-3}

In Table 4, the I_{corr} of the welded specimen with an alternating magnetic field is 2.64×10^{-8} A cm^{-2}, which is much lower than that of $I_{corr} = 1.82 \times 10^{-7}$ A cm^{-2} without an applied alternating magnetic field, and the E_{pass} is also significantly reduced after the magnetic field, which indicates that it is easier to form a stable passivation film. The increase in pitting potential indicates that the pitting resistance of the specimen is improved, and according to the I_{corr} calculation, the corrosion rate of the weld without magnetic field assistance is reduced from 0.00214 mm per year to 0.00028 mm per year. The above data indicate that the auxiliary effect of the alternating magnetic field not only makes it easier

to form a stable passivation film but also significantly reduces the corrosion sensitivity of the welded specimen and improves the pitting resistance of the weld. The improvement in corrosion resistance is mainly due to the introduction of an alternating magnetic field. The electromagnetic stirring action increases the proportion of austenite in the weld.

The relevance of the research for practical implementation:

The use of magnetic field-assisted duplex stainless steel narrow-gap laser arc hybrid welding can not only refine the grain but also improve the uniformity of the organization, which is very important to solve the real corrosion problems. In addition, the magnetic field is generated by a simple and portable magnetic field generator, which can be adapted to a variety of welding environments. It is useful for the generalization of this study in engineering.

4. Conclusions

This paper mainly investigates the effect of alternating magnetic fields on the organization and corrosion resistance of a narrow-gap laser arc hybrid weld of duplex stainless steel and analyzes the weld microstructure, fabrication distribution, grain size, etc. The main conclusions are as follows:

1. Welded joints without an applied magnetic field suffer from unfused and porosity defects and poor weld shaping. The weld is well formed and free of unfused and porosity defects with the assistance of a 40 mT alternating magnetic field. This is due to the fact that the presence of the magnetic field changes the heat distribution of the laser arc hybrid heat source in the narrow-gap space.
2. The two-phase homogeneity obtained by combining the two-phase contents of the four regions of the weld is 0.850, which is closer to 1.0 than the two-phase homogeneity of 0.657 in the absence of an alternating magnetic field. This indicates that the overall ratio of the two phases in the weld with the alternating magnetic field is more balanced than that without the magnetic field.
3. Under the effect of alternating magnetic fields, the austenite grain orientation distribution density is enhanced from 5.88 to 6.46 and the ferrite grain orientation distribution density is enhanced from 19.82 to 21.69. The texture density of austenite is increased, while the texture density of ferrite does not change significantly.
4. The ferrite and austenite phases are affected by the electromagnetic stirring effect of the applied magnetic field, and the average grain size of the austenite phase is reduced from 4.15 μm to 3.82 μm. The average grain size of the ferrite phase is reduced from 4.99 μm to 4.08 μm. The addition of the magnetic field results in the grain refinement of both phases. In addition, the density of twins in the tissue increases under the effect of an alternating magnetic field.
5. The electrochemical test results show that the corrosion resistance and passivation ability of the weld are improved under the magnetic field-assisted action. The Ecorr of the weld under the magnetic field-assisted condition is 75.2 mV higher than that in the absence of a magnetic field, and the Epit is 134.5 mV higher than that in the absence of a magnetic field. The corrosion rate is about 1/7th of that without the magnetic field. The increase in corrosion resistance depends mainly on austenite changes including the austenite grain size and content.
6. The quality of the weld is good with no unfused or porosity defects. Under the action of the magnetic field, the two phases are balanced, the organization is refined, and the corrosion resistance is improved. This provides support for the application of magnetic fields in the field of duplex stainless steel.

Author Contributions: Z.H.: Conceptualization, Investigation, Data curation, Experiments, Writing—original draft preparation. Y.Z.: Investigation, Supervision, Funding acquisition, Writing—review and editing. J.F.: Data curation, Supervision, Writing—review and editing. F.C.: Software, Experiments. G.C.: Supervision, Funding acquisition. Y.Q.: Investigation, Funding acquisition. All authors have read and agreed to the published version of the manuscript.

Funding: This research was funded by Jiangsu Postgraduate Research and Practice Innovation Program Project of China by SJCX23_2177.

Institutional Review Board Statement: Not applicable.

Informed Consent Statement: Written informed consent has been obtained from the co-authors to publish this paper.

Data Availability Statement: The data used to support the findings of this study are available from the corresponding author upon request.

Acknowledgments: The authors would like to thank the Jiangsu Postgraduate Research and Practice Innovation Program Project of China (SJCX23_2177) for the financial support of this paper.

Conflicts of Interest: The authors declare that they have no known competing financial interests or personal relationships that could have appeared to influence the work reported in this paper.

References

1. Rosado-Carrasco, J.; Krupp, U.; López-Morelos, V.H.; Giertler, A.; García-Rentería, M.A.; González-Sánchez, J. Effect of a Magnetic Field Applied during Fusion Welding on the Fatigue Damage of 2205 Duplex Stainless Steel Joints. *Int. J. Fatigue* **2019**, *121*, 243–251. [CrossRef]
2. Wu, J.; Cao, F.J.; Sun, T.; Huang, G.Q.; Li, M.S.; Hou, W.T.; Piao, Z.Y.; Shen, Z.K.; Shen, Y.F. Developing Ultrafine-Grained Structure with Balanced α/γ Fraction via Underwater Friction Stir Processing Enables Enhanced Wear and Corrosion Resistance of Duplex Stainless Steel. *Surf. Coat. Technol.* **2023**, *457*, 129295. [CrossRef]
3. Chaudhari, A.N.; Dixit, K.; Bhatia, G.S.; Singh, B.; Singhal, P.; Saxena, K.K. Welding Behaviour of Duplex Stainless Steel AISI 2205: A Review. *Mater. Today Proc.* **2019**, *18*, 2731–2737. [CrossRef]
4. Luo, J.; Yan, P.; Fan, Y.; Luo, S.; Long, Y. Investigation of Corrosion Behavior of 2205 Duplex Stainless Steel Coiled Tubing in Complex Operation Environments of Oil and Gas Wells. *Eng. Fail. Anal.* **2023**, *151*, 107355. [CrossRef]
5. Li, F.; Liu, Y.; Ke, W.; Jin, P.; Kong, H.; Chen, M.; Sun, Q. A Novel Pathway to Weld Forming Control and Microstructure Improvement of Duplex Stainless Steel via Alternating Magnetic Field. *J. Manuf. Process.* **2022**, *80*, 581–590. [CrossRef]
6. Wu, M.; Xin, R.; Wang, Y.; Zhou, Y.; Wang, K.; Liu, Q. Microstructure, Texture and Mechanical Properties of Commercial High-Purity Thick Titanium Plates Jointed by Electron Beam Welding. *Mater. Sci. Eng. A* **2016**, *677*, 50–57. [CrossRef]
7. Ning, J.; Zhang, L.-J.; Yang, J.; Yin, X.-Q.; Wang, X.-W.; Wu, J. Characteristics of Multi-Pass Narrow-Gap Laser Welding of D406A Ultra-High Strength Steel. *J. Mater. Process. Technol.* **2019**, *270*, 168–181. [CrossRef]
8. Sokolov, M.; Salminen, A.; Kuznetsov, M.; Tsibulskiy, I. Laser Welding and Weld Hardness Analysis of Thick Section S355 Structural Steel. *Mater. Des.* **2011**, *32*, 5127–5131. [CrossRef]
9. Cho, W.-I.; Woizeschke, P. Analysis of Molten Pool Behavior with Buttonhole Formation in Laser Keyhole Welding of Sheet Metal. *Int. J. Heat Mass Transf.* **2020**, *152*, 119528. [CrossRef]
10. Zhao, Y.; Wang, W.; Yan, K.; Liu, C.; Zou, J. Microstructure and Properties of Cu/Ti Laser Welded Joints. *J. Mater. Process. Technol.* **2018**, *257*, 244–249. [CrossRef]
11. Wang, J.; Sun, Q.; Zhang, T.; Zhang, S.; Liu, Y.; Feng, J. Arc Characteristics in Alternating Magnetic Field Assisted Narrow Gap Pulsed GTAW. *J. Mater. Process. Technol.* **2018**, *254*, 254–264. [CrossRef]
12. Raoelison, R.N.; Racine, D.; Zhang, Z.; Buiron, N.; Marceau, D.; Rachik, M. Magnetic Pulse Welding: Interface of Al/Cu Joint and Investigation of Intermetallic Formation Effect on the Weld Features. *J. Manuf. Process.* **2014**, *16*, 427–434. [CrossRef]
13. Rong, Y.; Huang, Y.; Xu, J.; Zheng, H.; Zhang, G. Numerical Simulation and Experiment Analysis of Angular Distortion and Residual Stress in Hybrid Laser-Magnetic Welding. *J. Mater. Process. Technol.* **2017**, *245*, 270–277. [CrossRef]
14. Yin, X.; Gou, J.; Zhang, J.; Sun, J. Numerical Study of Arc Plasmas and Weld Pools for GTAW with Applied Axial Magnetic Fields. *J. Phys. Appl. Phys.* **2012**, *45*, 285203. [CrossRef]
15. Li, L.; Huang, C.; Han, G.; Chen, R. Recent Progress on External Magnetic Field Assisted Laser Welding: Mechanism, Effect and Technology. *Int. J. Adv. Manuf. Technol.* **2023**, *125*, 1–23. [CrossRef]
16. Yang, C.; Yang, F.; Meng, X.; Putra, S.N.; Bachmann, M.; Rethmeier, M. Phase-Field Simulation of the Dendrite Growth in Aluminum Alloy AA5754 during Alternating Current Electromagnetic Stirring Laser Beam Welding. *Int. J. Heat Mass Transf.* **2024**, *218*, 124754. [CrossRef]
17. Yue, J.; Zhou, H.; Xie, C.; Zhou, W.; Liu, W. Temperature Field Simulation and Asymmetric Heat Transfer Distribution of Dissimilar Steel Welded with External Transverse Magnetic Field. *Mater. Today Commun.* **2023**, *37*, 107141. [CrossRef]
18. Tan, C.; Liu, Y.; Xu, B.; Wang, H.; Liu, F.; Gong, X.; Zeng, Z.; Chen, B.; Song, X. Numerical and Experimental Study of Thermal Fluid Flow and Keyhole Dynamic in Laser Welding of Aluminum Alloy Assisted by Electromagnetic Field. *Opt. Laser Technol.* **2023**, *157*, 108718. [CrossRef]
19. Fu, J.; Zhao, Y.; Zou, J.; Liu, X.; Pan, Y. Influence of the Magnetic Field on the Melting and Solidification Behavior of Narrow-Gap Laser Welding with Filler Wire. *Int. J. Adv. Manuf. Technol.* **2022**, *123*, 1123–1131. [CrossRef]

20. Ding, L.; Wang, H.; Zeng, Z.; Vladyslav, K.; Chen, L.; Li, F.; Zhang, Y.; Qin, B. The Influence Mechanism of Alternating Magnetic Field on Microstructure and Mechanical Properties of Ti-6Al-4V Alloy. *J. Mater. Eng. Perform.* **2023**. [CrossRef]
21. Xu, T.; Shi, Y.; Jiang, Z.; Liu, B.; Zhan, J.; Wang, Z. An Extraordinary Improvement in Cryogenic Toughness of K-TIG Welded 9Ni Steel Joint Assisted by Alternating Axial Magnetic Field. *J. Mater. Res. Technol.* **2023**, *25*, 3071–3077. [CrossRef]
22. García Rentería, M.A.; López Morelos, V.H.; García Hernández, R.; Curiel López, F.; Lemus-Ruíz, J. Effect on the Microstructure and Mechanical Properties of the Electromagnetic Stirring during GMA Welding of 2205 DSS Plates. *Mater. Sci. Forum* **2013**, *755*, 61–68. [CrossRef]
23. Li, F.; Liu, Y.; Jin, P.; Chen, M.; Ke, W.; Du, Y.; Liu, J.; Sun, Q. Appreciable-Tuned Ferrite/Austenite Phase Balance in the Fusion Zone of GTAW Welds via an Assisted Magnetic Field. *J. Alloys Compd.* **2021**, *885*, 160851. [CrossRef]
24. Liu, L.; Zhu, Y.; Liu, R. Study of Twin Tungsten Electrode—Wire Electrode Indirect Arc Welding Assisted by Alternating Magnetic Field. *J. Manuf. Process.* **2023**, *101*, 171–180. [CrossRef]
25. Zhu, Z.; Ma, X.; Wang, C.; Mi, G. Grain Refinement and Orientation Alternation of 10 mm 316L Welds Prepared by Magnetic Field Assisted Narrow Gap Laser-MIG Hybrid Welding. *Mater. Charact.* **2020**, *164*, 110311. [CrossRef]
26. Thakur, A.; Kumar, A.; Sharma, S.; Ganjoo, R.; Assad, H. Computational and Experimental Studies on the Efficiency of Sonchus Arvensis as Green Corrosion Inhibitor for Mild Steel in 0.5 M HCl Solution. *Mater. Today Proc.* **2022**, *66*, 609–621. [CrossRef]
27. García-Rentería, M.A.; López-Morelos, V.H.; González-Sánchez, J.; García-Hernández, R.; Dzib-Pérez, L.; Curiel-López, F.F. Effect of Electromagnetic Interaction during Fusion Welding of AISI 2205 Duplex Stainless Steel on the Corrosion Resistance. *Appl. Surf. Sci.* **2017**, *396*, 1187–1200. [CrossRef]
28. Zhong, Y.; Zheng, Z.; Li, J.; Wang, C. Effect of In-Situ Transverse Magnetic Field on Microstructure, Mechanical Properties and Corrosion Resistance of the Directed Energy Deposited 316L Stainless Steel. *Addit. Manuf.* **2023**, *68*, 103508. [CrossRef]
29. Wang, L.; Ma, Y.; Xu, J. Numerical Simulation of Arc-Droplet-Weld Pool Behaviors during the External Magnetic Field-Assisted MIG Welding-Brazing of Aluminum to Steel. *Int. J. Therm. Sci.* **2023**, *194*, 108530. [CrossRef]
30. Zhu, Z.; Ma, X.; Mi, G.; Wang, C. Electron Microscopy Study of Laser Welded GH909 Superalloy Joint. *J. Mater. Res. Technol.* **2020**, *9*, 15525–15536. [CrossRef]
31. Santos, R.M.; Rodrigues, D.G.; Dias Santos, M.L.; Santos, D.B. Martensite Reversion and Strain Hardening of a 2304 Lean Duplex Stainless Steel Subjected to Cold Rolling and Isochronous Annealing at Low Temperatures. *J. Mater. Res. Technol.* **2022**, *16*, 168–186. [CrossRef]
32. Cai, B.; Fu, J.; Zhao, Y.; Chen, F.; Qin, Y.; Song, S. Effect of Alternating Magnetic Field on Arc Plasma Characteristics and Droplet Transfer during Narrow Gap Laser-MIG Hybrid Welding. *Metals* **2021**, *11*, 1712. [CrossRef]
33. Fu, J.; Rao, Z.; Zhao, Y.; Zou, J.; Liu, X.; Pan, Y. Microstructure and Texture Characterization of Duplex Stainless Steel Joints Welded by Alternating Magnetic Field-Assisted Hybrid Laser-GMAW Welding. *Materials* **2022**, *15*, 8741. [CrossRef]
34. Cui, S.; Pang, S.; Pang, D.; Zhang, Z. Influence of Welding Speeds on the Morphology, Mechanical Properties, and Microstructure of 2205 DSS Welded Joint by K-TIG Welding. *Materials* **2021**, *14*, 3426. [CrossRef]
35. You, J.; Li, Z.; Li, Y.; Cai, Z. Microstructure and Properties of Underwater Wet Laser Welded 0Cr25Ni6Mo3N Duplex Stainless Steel Joints. *Mater. Today Commun.* **2023**, *36*, 106622. [CrossRef]
36. Sun, Y.; Tan, X.; Lan, R.; Ran, G.; Li, J.; Jiang, Y. Mechanisms of Inclusion-Induced Pitting of Stainless Steels: A Review. *J. Mater. Sci. Technol.* **2024**, *168*, 143–156. [CrossRef]